

Energy of the excess electron in methane and ethane near the critical point

Xianbo Shi ^{a,b}, Luxi Li ^{a,b}, G. L. Findley ^c, C. M. Evans ^{a,b,*}

^a*Department of Chemistry and Biochemistry, Queens College – CUNY, Flushing, NY 11367, United States*

^b*Department of Chemistry, Graduate Center – CUNY, New York, NY 10016, United States*

^c*Department of Chemistry, University of Louisiana at Monroe, Monroe, LA 71209, United States*

Abstract

Field ionization measurements of trimethylamine in methane and triethylamine in ethane are presented as a function of perturber number density at various noncritical temperatures and near the perturber critical isotherm. Critical point effects are observed that are similar to those seen in atomic fluids. A two-Yukawa potential is shown to model the perturber/perturber interactions accurately by calculating the phase diagram of the perturber fluids, and using this potential the local Wigner-Seitz model for the energy of the excess electron is successfully applied to these molecular systems.

Key words: Wigner-Seitz model, supercritical alkanes, field ionization, quasi-free electron energy, critical point effects

PACS: 33.15.Ry, 34.30.+h, 31.70.-f, 31.70.Dk

1 Introduction

The perturber induced shift $\Delta(\rho_P)$ [$\rho_P \equiv$ perturber number density] in the ionization energy of various dopants in dense atomic perturbers has been investigated recently using field ionization [1–8]. The energy of the excess electron $V_0(\rho_P)$ in a perturber [i.e., the minimum energy of the conduction band of the perturbing medium] can be extracted from $\Delta(\rho_P)$ using [1–8]

$$V_0(\rho_P) = \Delta(\rho_P) - P_+(\rho_P), \quad (1)$$

where $P_+(\rho_P)$ is the ensemble average dopant core/perturber polarization energy. We have shown that both $\Delta(\rho_P)$ and $V_0(\rho_P)$ increase significantly near the critical temperature and density of the attractive (i.e., negative electron scattering length A) rare gas perturbers argon [2,3], krypton [4] and xenon [5]. This critical point effect, as well as the overall perturber density dependance of $\Delta(\rho_P)$ and $V_0(\rho_P)$ [1,5], was accurately described using the local Wigner-Seitz model [1,7,8], given by

$$\begin{aligned} V_0(\rho_P) &= P_-(\rho_P) + E_k(\rho_P) + \frac{3}{2} k_B T, \\ \Delta(\rho_P) &= P_+(\rho_P) + V_0(\rho_P). \end{aligned} \quad (2)$$

In eq. (2), $P_-(\rho_P)$ is the ensemble average electron/perturber polarization energy, $E_k(\rho_P)$ is the zero-point kinetic energy of the quasi-free electron, and $(3/2)k_B T$ [$k_B \equiv$ Boltzmann's constant] is the thermal energy of the quasi-free electron.

* Corresponding author.

Email addresses: xianbo.shi@qc.cuny.edu (Xianbo Shi), lu.li@qc.cuny.edu (Luxi Li), findley@ulm.edu (G. L. Findley), cherice.evans@qc.cuny.edu (C. M. Evans).

In this Letter, we extend the local Wigner-Seitz model to the simple alkanes methane and ethane. The quasi-free electron energy $V_0(\rho_P)$ [9–15] and the electron mobility [16–22], which depends upon $V_0(\rho_P)$, have been widely investigated in the attractive simple alkanes. Methane is of interest in the present study because it is an attractive molecular perturber of high symmetry and can therefore be considered as an analogue of an attractive rare gas. Ethane, on the other hand, was selected because photoinjection measurements of $V_0(\rho_P)$ [10–15] showed significant differences in comparison to those of methane [9–12]. The most striking of these differences is that $V_0(\rho_P)$ becomes positive at ethane number densities greater than $\sim 9.0 \times 10^{21} \text{ cm}^{-3}$, while that in methane remains negative up to the density of the triple point liquid. Moreover, critical point effects on the excess electron energy have not been investigated in either of these molecular fluids. Therefore, we present new field ionization results for trimethylamine (TMA) in methane and triethylamine (TEA) in ethane at noncritical temperatures and on an isotherm near the perturber critical isotherm. We also demonstrate that appropriate spherical intermolecular potentials can be selected for these perturbers by comparing calculated phase diagrams to those obtained from empirical perturber equations of state. We then show that the local Wigner-Seitz model reproduces $\Delta(\rho_P)$ and $V_0(\rho_P)$ in methane and ethane to within experimental error using these same intermolecular potentials.

2 Experimental

TMA (trimethylamine, Matheson Gas Products, 99.5%), TEA (triethylamine, Sigma-Aldrich, 99.8%), methane (Matheson Gas Products, 99.999%) and ethane

(Matheson Gas Products, 99.995%) were used without further purification. The absence of impurities in the spectral range of interest was verified by checking photoionization and absorption spectra for each dopant and perturber. The gas handling system (GHS) and the general procedure used to achieve a homogenous mixture for each sample have been described previously [8,24]. Prior to the introduction of any sample, the GHS was baked to a base pressure of low 10^{-8} Torr; after adding the dopant, the GHS was allowed to return to the low 10^{-7} Torr range prior to introducing the perturber. Cross contamination was avoided by baking the GHS to the base pressure of low 10^{-8} Torr before introducing a new dopant/perturber system. In all cases the dopant concentration was < 10 ppm.

Photoionization spectra were measured with monochromatic synchrotron radiation [23,24] having a resolution of 1.8 \AA (or 10 meV in the spectral region investigated). Two different copper sample cells [8,23,24] were used in these experiments: Cell 1, which was used for both methane and ethane, is equipped with entrance and exit MgF_2 windows and a pair of parallel plate electrodes (stainless steel, 3.0 mm spacing) oriented parallel to the incoming radiation and perpendicular to the windows. The light path inside Cell 1 is 1.0 cm. Cell 2, which was used principally for signal enhancement along the critical isotherm in ethane, is equipped with an entrance LiF window coated with a thin (7 nm) layer of gold to act as an electrode. The second electrode (stainless steel) is placed parallel to the window with a spacing of 1.0 mm. Both cells, each of which was designed to withstand gas pressures up to 100 bar, gave comparable results. The temperature was maintained to $\pm 0.5^\circ\text{C}$ at noncritical temperatures and to $\pm 0.3^\circ\text{C}$ at the critical temperature using an open flow liquid nitrogen cryostat and resistive heater attached to the sample cell.

A field ionization spectrum is obtained by subtracting a photoionization spectrum measured at a low DC electric field F_L from a spectrum measured at a high DC electric field F_H after intensity normalization (necessary to remove the effects of secondary ionization [25]). The field ionization spectrum results from high- n Rydberg states that are field ionized by F_H but not by F_L . As exemplified in Fig. 1 for pure methyl iodide [8], a variation in the strength of the electric fields leads to a shift in the energetic position of the field ionization peak, with the shift being linearly dependent on $\sqrt{F_L} + \sqrt{F_H}$. F_H and F_L are adjusted to optimize the dopant field ionization spectrum at each perturber number density. (The electric fields are also selected to saturate the photocurrent, while remaining below those field strengths leading to dielectric breakdown via collisional ionization. For the data reported here, the photocurrents were of the order of 10^{-10} A.)

At any given perturber density, the perturber induced shift of the dopant ionization energy is obtained from [1]

$$\Delta(\rho_P) = I_F(\rho_P) + c_D \left(\sqrt{F_L} + \sqrt{F_H} \right) - I_g, \quad (3)$$

where $I_F(\rho_P)$ is the dopant ionization energy perturbed by the electric field and by the dense gas, c_D is a dopant-dependent/perturber-independent positive constant, and I_g is the gas phase dopant ionization energy. The field ionization constant c_D and the gas phase dopant ionization energy I_g are empirically determined from field ionization studies [8] of the neat dopant at various electric field strengths. These field ionization measurements gave $c_D = 2.8 \pm 0.2 \times 10^{-4}$ eV cm^{1/2} V^{-1/2} and $I_g = 8.370 \pm 0.008$ eV for TMA; for TEA, $c_D = 4.9 \pm 0.3 \times 10^{-4}$ eV cm^{1/2} V^{-1/2} and $I_g = 7.833 \pm 0.015$ eV. The total error for $\Delta(\rho_P)$ presented here is given by a sum of the field correc-

tion error, the goodness-of-fit error (for fitting a field ionization spectrum to a Gaussian line shape), and the error arising from the energy uncertainty due to the resolution of the monochromator (i.e., ± 5 meV). This total experimental error is between 0.030 and 0.040 eV.

3 Results and Discussion

In the local Wigner-Seitz model [i.e., eq. (2)], the average polarization energies are determined using a standard statistical mechanical model [1,7,8]:

$$P_{\pm}(\rho_P) = -4\pi\rho_P \int_0^{\infty} g(r) w_{\pm}(r) r^2 dr . \quad (4)$$

where $g(r)$ is the dopant/perturber radial distribution function (RDF) $g_{PD}(r)$, or the perturber/perturber RDF $g_{PP}(r)$, for the calculation of $P_+(\rho_P)$ or $P_-(\rho_P)$, respectively. The interaction potential $w_{\pm}(r)$ can be written as a sum of pairwise potentials [1,7,8]

$$w_{\pm}(r) = -\frac{1}{2} \alpha_P e^2 \sum_i^N r_i^{-4} f_{\pm}(r_i) , \quad (5)$$

where $f_{\pm}(r)$ is a screening function accounting for the repulsive interactions between induced dipoles in the perturber, e is the electron charge, and α_P is the perturber polarizability. For the quasi-free electron/perturber interaction, the screening function $f_-(r)$ is sensitive to the perturber/perturber interactions and, therefore, is a function of $g_{PP}(r)$. The screening function $f_+(r)$, on the other hand, models the induced dipoles in the perturbing fluid generated by the dopant cation/perturber interactions. This screening function must therefore incorporate $g_{PP}(r)$ to account for perturber induced dipole/induced dipole interactions, as well as $g_{PD}(r)$ for the dopant/perturber interactions.

Thus, any critical point behavior in $P_{\pm}(\rho_P)$ arises from variations in $g_{PP}(r)$ and $g_{PD}(r)$ near the critical density and temperature.

The zero-point kinetic energy $E_k(\rho_P)$ of the quasi-free electron is obtained from solving the Schrödinger equation [7,8]

$$\nabla^2\psi + \frac{2m_e}{\hbar^2} [E_k - V_{\text{loc}}(r)] \psi = 0 \quad (6)$$

for the quasi-free electron in a dense perturber. In eq. (6), $V_{\text{loc}}(r)$ is a short-ranged potential that accounts for local dynamic polarization of a perturber by the optical electron, m_e is the mass of the electron, and \hbar is the reduced Planck constant. The local potential $V_{\text{loc}}(r)$ satisfies an average translational symmetry given by [7,8]

$$V_{\text{loc}}(r) = V_{\text{loc}}(r + 2r_b) , \quad (7)$$

where r_b is the interaction range. At any density, the minimum distance between a quasi-free electron with low kinetic energy and a single perturber is given by the absolute value of the scattering length A . At high perturber number densities, under the assumption that interactions in the first solvent shell dominate the dynamics of the problem, the maximum distance r_{ℓ} for a short-ranged interaction is one-half of the spacing between two perturbers in the first solvent shell. This maximum spacing, otherwise known as the local Wigner-Seitz radius, is given by [1,7,8]

$$r_{\ell} \equiv \sqrt[3]{\frac{3}{4\pi g_{\text{max}} \rho_P}} , \quad (8)$$

where g_{max} is the maximum of $g_{PP}(r)$. Thus, the interaction range for the local short-ranged potential is $r_b = r_{\ell} - |A|$. By applying these conditions to the asymptotic solutions of eq. (6), the zero-point kinetic energy of the quasi-free

electron is [7,8]

$$E_k(\rho_P) = \frac{\hbar^2 \eta_0^2}{2 m_e (r_\ell - |A|)^2} . \quad (9)$$

In eq. (9), η_0 is the phase shift induced by the short-ranged potential, and the density dependence arises from r_ℓ . (The critical point behavior in $E_k(\rho_P)$ results from a decrease in r_ℓ near the critical density along the critical isotherm due to density fluctuations.) Finally, as will be shown below, the assumption that s -wave scattering predominates, which is implicit in eq. (6), is justified by $k r_b = \eta_0 < 1$, where $k = [2 m_e E_k(\rho_P)/\hbar^2]^{1/2}$

Since the determination of $P_\pm(\rho_P)$ involves $g_{PP}(r)$ and $g_{PD}(r)$, while r_ℓ is ascertained from the maximum of $g_{PP}(r)$, accurately calculating the RDFs for each dopant/perturber system over a large density and temperature range is very important. In order to minimize numerical instabilities in determining the RDFs at high densities near the perturber triple point, as well as along isotherms close to the critical temperature, different methods for numerically integrating the Ornstein-Zernike relation with different closures have been compared [8,26–29]. The direct integration of the Percus-Yevick equation [26] for binary systems provided the most stable and reliable results [8] when used with an optimization routine developed by Ng *et al.* [29]. (This optimization routine employed a weighted linear combination of $m \geq 3$ previous iterations to generate the input for the $(m + 1)^{th}$ iteration.) This direct integration [26] leads to a set of four coupled integro-differential equations, which reduces to a set of two coupled equations for the dilute binary systems considered here (i.e., dopant concentration < 10 ppm).

One of the goals of this study was to assess the adequacy of spherical intermolecular potentials for modeling dopant/perturber and perturber/perturber

interactions in selected dense molecular fluids. We chose to use the two-Yukawa (TY) potential

$$U(r) = \begin{cases} \infty, & r < R, \\ -\kappa_0 \varepsilon r^{-1} [e^{-z_1(r-\sigma)} - e^{-z_2(r-\sigma)}], & r \geq R, \end{cases} \quad (10)$$

because it allowed us to vary the collision radius σ , the well-depth $\kappa_0\varepsilon$ and the steepness of the attractive z_1 and repulsive z_2 tails independently. (R is a hard core radius that defines the minimum distance between spherical perturbers.) Moreover, by an appropriate choice of parameters, the TY potential can mimic any of the other spherical potentials (e.g., the Lennard-Jones 6-12 potential [30]). However, the large number of potential parameters requires the availability of additional data. For simplicity, we chose to validate the perturber/perturber intermolecular potential, along with the determined radial distribution function, by comparing the calculated equation of state, generated from [31]

$$\frac{p}{k_B T} = \rho_P - \frac{2\pi\rho_P}{3k_B T} \int_0^\infty r^3 \frac{dU_{PP}(r)}{dr} g_{PP}(r) dr, \quad (11)$$

with experimental thermodynamic data. These data were obtained from the empirical equations of state for the perturber, namely the Modified Benedict-Webb-Rubin (MBWR) equation of state for methane [32] at any temperature, and for ethane at temperatures between -68°C and -51°C [33], and the Schmidt-Wagner (SW) equation of state for ethane at any other temperature [34]. Fig. 2 presents the calculated pressure p (open markers) as a function of the perturber number density ρ_P in comparison to the experimental pressures (solid markers) for the density/temperature data sets used in our investigations. Clearly, the spherical two-Yukawa potential (cf. Table 1 for parameters) suitably models the equation of state for the highly symmetric methane and

the less symmetric ethane. This correspondence also indicates that the radial distribution functions obtained from the coupled Percus-Yevick equations are valid for these molecular perturbers. (We should note that the larger error that appears at higher number densities could be caused by the isotherm steepness as well as by a failure of the spherical approximation in this region.)

Once the perturber/perturber intermolecular potential was determined from fitting the thermodynamic equation of state, $V_0(\rho_P)$ from photoinjection measurements for each perturber [9,10,13,14] was fitted to [1,7,8]

$$V_0(\rho_P) = P_-(\rho_P) + \frac{3}{2}k_B T + \frac{\hbar^2 \eta_0^2}{2m_e(r_\ell - |A|)^2} \quad (12)$$

by adjusting A and η_0 . In order to calculate $P_+(\rho_P)$, the dopant/perturber interaction was treated with a modified Stockmeyer potential,

$$V(r) = 4\varepsilon' \left[\left(\frac{\sigma'}{r} \right)^{12} - \left(\frac{\sigma'}{r} \right)^6 \right] - \frac{1}{r^6} \alpha_P \mu_D^2, \quad (13)$$

which can be rewritten in standard Lennard-Jones 6-12 (LJ6-12) form [1] with the parameters

$$\varepsilon = \varepsilon' \left[1 + \alpha_P \mu_D^2 / (4\varepsilon' \sigma'^6) \right]^2$$

and

$$\sigma = \sigma' \left[1 + \alpha_P \mu_D^2 / 4\varepsilon' \sigma'^6 \right]^{-1/6}.$$

The dopant/perturber intermolecular potential parameters, which are used to calculate the RDFs necessary for determining $P_+(\rho_P)$ in eq. (2), were adjusted in comparison to the experimental $\Delta(\rho_P)$. Small modifications (within 2%) were then made to A and η_0 in order to improve the overall fit to the measured $\Delta(\rho_P)$. (These small adjustments were necessary because of the large scatter in the photoinjection data [9,10,13,14] for $V_0(\rho_P)$.) Table 1 lists all of the intermolecular potential parameters used in calculating the radial distribution

functions necessary for determining $V_0(\rho_P)$ and $P_+(\rho_P)$, while Table 2 gives the scattering length A and the phase shift η_0 .

Fig. 3 compares the calculated (solid lines) and measured (markers) $\Delta(\rho_P)$ for TMA in methane and TEA in ethane. Clearly, the calculated $\Delta(\rho_P)$ closely matches experiment, with a scatter that falls within the experimental error for both systems. [The lack of a theoretical result at the highest methane density is due to our inability to stabilize the RDF calculation there. In order to show the trend in $\Delta(\rho_P)$ in ethane, one more calculated point at the density of $9.6 \times 10^{21} \text{ cm}^{-3}$ is presented in the region where field ionization results are unavailable because of strong ethane absorption.] Fig. 3 also presents the quasi-free electron energy $V_0(\rho_P)$ obtained from the local Wigner-Seitz model (lines) in comparison to experiment (markers). Eq. (1) was used to determine the empirical $V_0(\rho_P)$, while the calculated $V_0(\rho_P)$ comes from eq. (2). Similar to the previous photoinjection results [9,10,13,14] at noncritical temperatures, the new field ionization measurements and calculations of TMA in methane give a negative $V_0(\rho_P)$ for all methane densities, indicative of the existence of a quasi-free electron in the conduction band of methane. $V_0(\rho_P)$ in ethane, on the other hand, is negative at low to medium densities and then becomes positive at densities greater than $8.0 \times 10^{21} \text{ cm}^{-3}$. (The results presented here have less scatter than do the photoinjection measurements, thereby allowing one to determine the density where $V_0(\rho_P) > 0$ with more accuracy.) In order to understand these results, we must consider the density dependence of the individual components of $V_0(\rho_P)$ and $\Delta(\rho_P)$.

Fig. 4 shows the average ion/perturber polarization energy $P_+(\rho_P)$, the average electron/perturber polarization energy $P_-(\rho_P)$, and the zero-point kinetic energy $E_k(\rho_P)$ for methane and ethane at noncritical temperatures and on an

isotherm near the critical isotherm of the perturber. One should notice in Fig. 4a that the average ion/perturber polarization energy is smaller for TMA⁺ in methane than for TEA⁺ in ethane. When comparing the dopant/perturber intermolecular potential parameters in Table 1, the collision radius σ for the TMA/methane interaction is large, indicating that the dopant/perturber interaction is relatively small. Since methane is a non-polar solvent while TMA is a polar dopant, TMA may be only partially soluble in methane, thereby leading to the shallow $P_+(\rho_{\text{Me}})$. Because the TMA/methane interaction is weak, the well-depth for the intermolecular potential should also be small. For the calculations presented in Figs. 3 and 4, we chose a well-depth of $\varepsilon/k_B = 125.0$ K, which ensured numerical stability for the determination of the RDFs in methane at higher densities. On the other hand, since ethane has a much larger polarizability than does methane, the dipole-induced dipole interaction between TEA and ethane is not significantly weaker than the TEA/TEA or ethane/ethane interactions. Therefore, the collision radius σ for the TEA/ethane interaction is smaller and the well-depth is larger than are those for the TMA/methane interaction. These stronger dopant/perturber interactions for TEA in ethane lead to the much steeper $P_+(\rho_{\text{Et}})$.

The average electron/perturber polarization energy shown in Fig. 4b is slightly larger in methane than in ethane. The electron/perturber polarization energy is dominated by the perturber/perturber interactions. As one would expect, the induced dipole/induced dipole interactions in methane are weaker than are those in ethane. Thus, the well depth for methane is smaller than that for ethane. However, the overall size of the electron/perturber polarization energy is dominated by the collision radius, which determines the most probable distance between perturber molecules. A small radius indicates that the

perturbers can pack closer together at higher densities. This, in turn, increases the local density which gives a larger overall shift in the electron/perturber polarization energy.

The zero-point kinetic energy $E_k(\rho_P)$ of the quasi-free electron, shown in Fig. 4c, is dependent on the local density within the first solvent shell through the local Wigner-Seitz radius. Fig. 5 presents the maximum local density in the first solvent shell (i.e., $\rho_{\text{loc}} = g_{\text{max}}\rho_P$) plotted as a function of reduced perturber number density. Fig. 5 clearly indicates that this local density is larger for methane than for ethane, which is not surprising given the size difference of these two molecules. However, $E_k(\rho_P)$ increases more for ethane than for methane at higher perturber number densities (cf. Fig. 4c), which is caused by the larger electron scattering length in ethane. The electron scattering length represents the minimum distance between the electron and a single perturber, while the local Wigner-Seitz radius represents the maximum distance between the electron and a single perturber in the Wigner-Seitz cell. Thus, the difference between these two distances is the size of the “box” in which the quasi-free electron is confined during the electron/perturber interaction. At higher perturber number densities, the electron/ethane interaction box size is smaller and, therefore, the zero-point kinetic energy of the electron is larger in ethane.

Fig. 4 also clearly shows those effects that dominate near the critical point. The ensemble average polarization energies $P_{\pm}(\rho_P)$ show only a slight difference near the perturber critical point. The zero-point kinetic energy $E_k(\rho_P)$, on the other hand, has a significant critical point effect. As was seen for atomic perturbers [1–8], the local density (cf. Fig. 5) in the first solvent shell increases because of larger perturber/perturber correlations near the critical

point. As discussed above, this local density increase also decreases the electron/perturber interaction box size and, therefore, increases $E_k(\rho_P)$ near the critical point of the perturber.

In this Letter, field ionization measurements of trimethylamine in methane and triethylamine in ethane have been reported. We showed that a spherically symmetric intermolecular potential (i.e., the two-Yukawa potential) reproduced the pressure/density phase diagrams for both methane and ethane with an appropriate choice of the intermolecular potential parameters. Using this intermolecular potential, we were able to extend successfully the local Wigner-Seitz model to molecular perturbers. The enhancement in the local density near the perturber critical point was shown to lead to a large increase in $E_k(\rho_P)$ which, in turn, dominates the observed critical point effect in $V_0(\rho_P)$ and $\Delta(\rho_P)$.

Acknowledgements

The experimental measurements reported here were performed at the University of Wisconsin Synchrotron Radiation Center (NSF DMR-0537588). We thank Ms. Gina M. Moriarty (Queens College – CUNY) for her assistance in these measurements. This work was supported by grants from the Petroleum Research Fund (45728-B6), from the Professional Staff Congress - City University of New York (60074-34 35) and from the Louisiana Board of Regents Support Fund (LEQSF(2006-09)-RD-A33).

References

- [1] C. M. Evans, G. L. Findley, *Phys. Rev. A* 72 (2005) 022717.
- [2] C. M. Evans, G. L. Findley, *Chem. Phys. Lett.* 410 (2005) 242.
- [3] C. M. Evans, G. L. Findley, *J. Phys. B: At. Mol. Opt. Phys.* 38 (2005) L269.
- [4] Luxi Li, C. M. Evans, G. L. Findley, *J. Phys. Chem. A* 109 (2005) 10683.
- [5] Xianbo Shi, Luxi Li, C. M. Evans, G. L. Findley, *Chem. Phys. Lett.* 432 (2006) 62.
- [6] Xianbo Shi, Luxi Li, C. M. Evans, G. L. Findley, *Nucl. Inst. Meth. A* 582 (2007) 270.
- [7] Xianbo Shi, Luxi Li, Gina M. Moriarty, C. M. Evans, G. L. Findley, *Chem. Phys. Lett.* 454 (2008) 12.
- [8] Xianbo Shi, Ph.D. dissertation, The Graduate Center of the City University of New York, NY, 2009.
- [9] U. Asaf, R. Reininger, I. T. Steinberger, *Chem. Phys. Lett.* 100 (1983) 363.
- [10] W. Tauchert, H. Jungblut, W. F. Schmidt, *Can. J. Chem.* 55 (1977) 1860.
- [11] S. Noda, L. Kevan, *J. Chem. Phys.* 61 (1974) 2467.
- [12] A. Krasinsky, U. Asaf, I. T. Steinberger, R. Reininger, *Chem. Phys. Lett.* 231 (1994) 536.
- [13] Y. Yamaguchi, T. Nakajima, M. Nishikawa, *J. Chem. Phys.* 71 (1979) 550.
- [14] S. Noda, L. Kevan, K. Fueki, *J. Phys. Chem.* 79 (1975) 2866.
- [15] H. Faidas, L. G. Christophorou, P. G. Datskos, D. L. McCorkle, *J. Chem. Phys.* 90 (1989) 6619.

- [16] R. A. Holroyd in: Charged Particle and Photon Interactions with Matter, A. Mozumder and Y. Hantano, eds., Marcel Dekker, New York, 2003, and references therein.
- [17] N. Gee, G. R. Freeman, *Phys. Rev. A* 20 (1979) 1152.
- [18] J. -P. Dodelet, G. R. Freeman, *Can. J. Chem.* 55 (1977) 2264.
- [19] M. G. Robinson, G. R. Freeman, *Can. J. Chem.* 52 (1974) 440.
- [20] L. G. Christophorou, D. L. McCorkle, *Chem. Phys. Lett.* 42 (1976) 533.
- [21] M. Nishikawa, K. Fueki, *Chem. Phys. Lett.* 83 (1981) 301.
- [22] W. H. Hamil, *J. Phys. Chem.* 85 (1981) 2071.
- [23] C.M. Evans, J.D. Scott, G.L. Findley, *Rec. Res. Dev. Chem. Phys.* 3 (2002) 351, and references therein.
- [24] C. M. Evans, Ph.D. dissertation, Louisiana State University, LA, 2001.
- [25] A. K. Al-Omari, Ph.D. dissertation, University of Wisconsin Madison, WI, 1996.
- [26] E. W. Grundke, D. Henderson, R. D. Murphy, *Can. J. Phys.* 51 (1973) 1216.
- [27] M. J. Gillan, *Molec. Phys.* 38 (1979) 1781.
- [28] S. Labík, A. Malijevský, P. Voňka, *Molec. Phys.* 56 (1985) 709.
- [29] K-C. Ng, *J. Chem. Phys.* 61 (1974) 2680.
- [30] Y. Tang, Z. Tong, B. C. -Y. Lu, *Fluid Phase Equilib.* 134 (1997) 21.
- [31] D. McQuarrie, *Statistical Mechanics*, Harper & Row, New York, 1976.
- [32] B. A. Younglove, J. F. Ely, *J. Phys. Chem. Ref. Data* 16 (1987) 577.
- [33] D. G. Friend, H. Ingham, J. F. Ely, *J. Phys. Chem. Ref. Data* 20 (1991) 275.
- [34] R. Schmidt, W. Wagner, *Fluid Phase Equilib.* 19 (1985) 175.

Table 1

Intermolecular potential parameters used in calculating radial distribution functions.

	σ (Å)	ε/k_B (K)	κ_0 (Å)	z_1 (Å ⁻¹)	z_2 (Å ⁻¹)
CH ₄ -CH ₄ (TY)	3.300	143.5	8.500	0.900	4.250
C ₂ H ₆ -C ₂ H ₆ (TY)	4.015	253.8	8.500	0.685	3.500
TMA-CH ₄ (LJ6-12)	6.500	125.0	–	–	–
TEA-C ₂ H ₆ (LJ6-12)	5.100	230.0	–	–	–

Table 2

The zero-kinetic-energy electron scattering length A and the phase shift η_0 used in the local Wigner-Seitz model calculations for methane and ethane.

Perturber	A (Å)	η_0
CH ₄	-0.826 ± 0.004	0.463 ± 0.003
C ₂ H ₆	-1.655 ± 0.005	0.321 ± 0.003

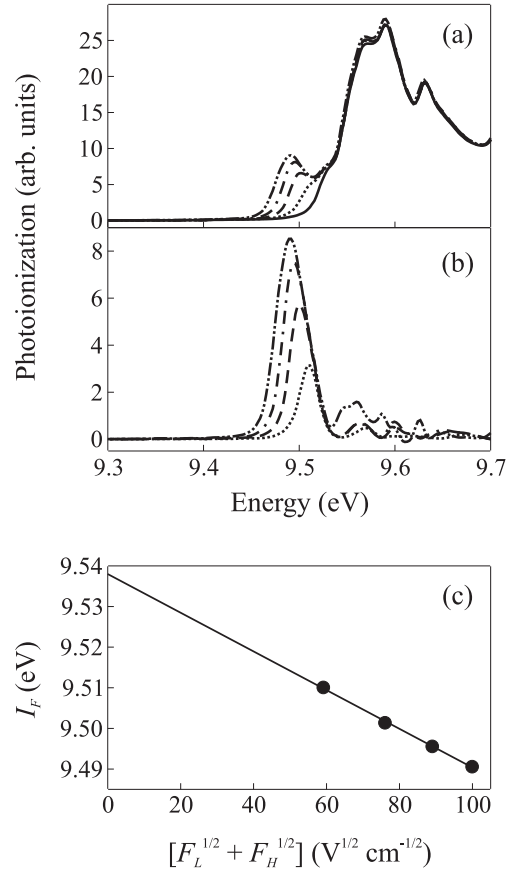


Fig. 1. An example field ionization study of 0.10 mbar CH₃I [8]. (a) Photoionization spectra at (—) 333 V/cm, (···) 1667 V/cm, (- - -) 3333 V/cm, (- · -) 5000 V/cm, and (- · · -) 6667 V/cm after intensity normalization, necessary to correct for secondary ionization. (b) Field ionization spectra obtained with $F_L = 333$ V/cm and with various F_H [see (a)]. (c) The energy I_F of the field ionization peak plotted as a function of the square root of the electric fields. See text for discussion.

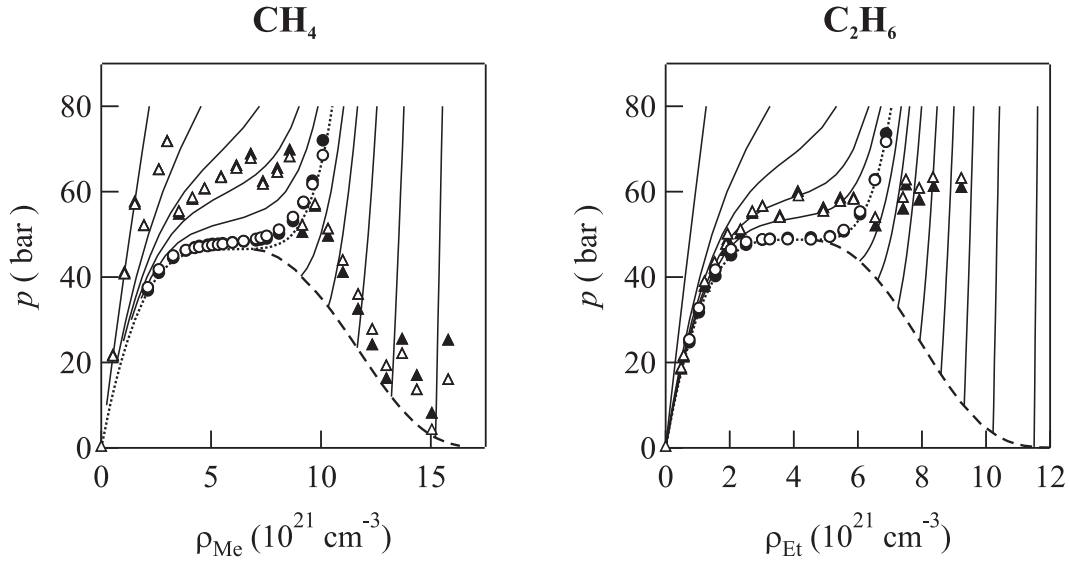


Fig. 2. The pressure/density phase diagram of CH_4 and C_2H_6 for the MBWR and SW equations of state (see text for details) showing several noncritical isotherms (—), the critical isotherm (\cdots), and the vapor pressure curve (- - -). (\blacktriangle , \bullet) present thermodynamic conditions for selected noncritical and critical experimental field ionization data, respectively. (Δ and \circ) present calculated thermodynamic conditions for noncritical temperatures and along the critical isotherm, respectively. The calculated values were obtained from eq. (11) with the potential parameters given in Table 1.

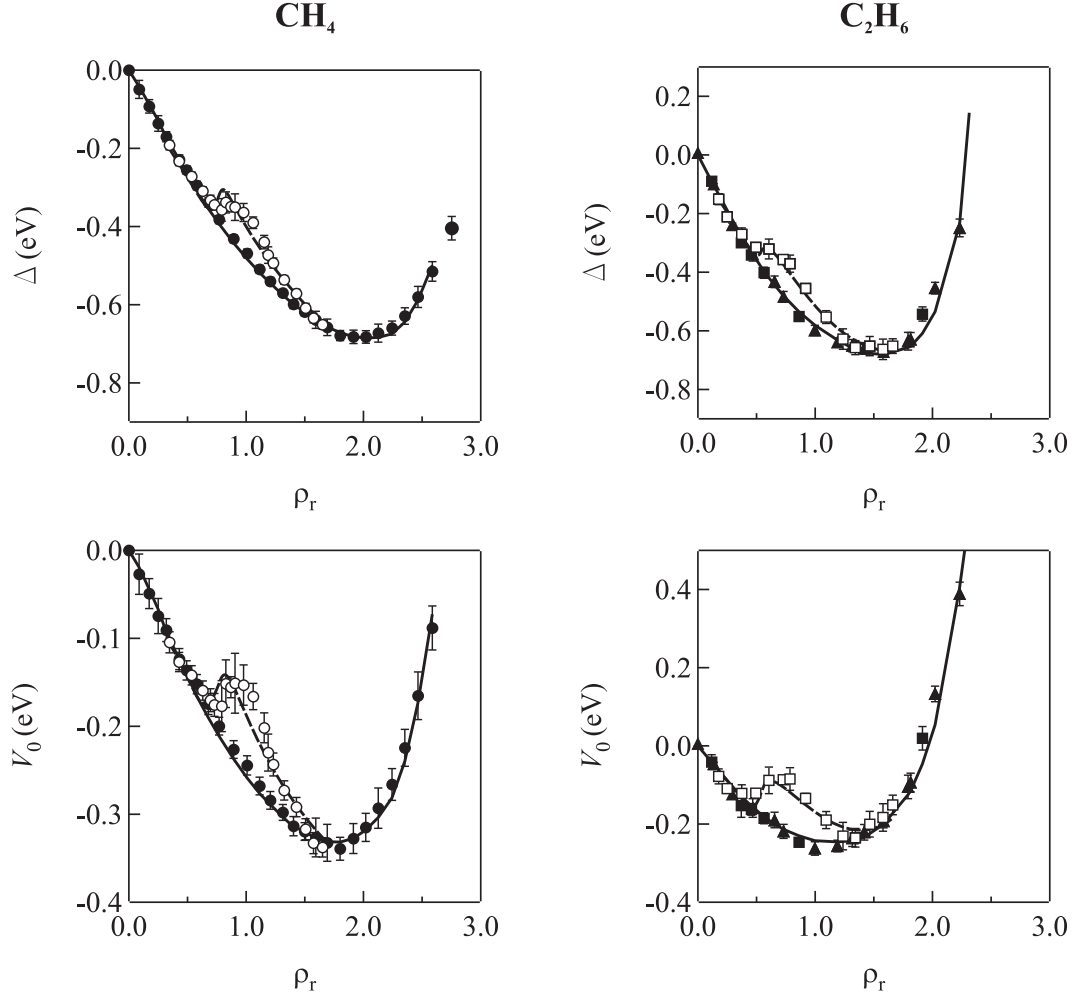


Fig. 3. Comparison of experiment (markers) and calculation (lines) for the perturber-induced dopant ionization energy $\Delta(\rho_P)$, and for the quasi-free electron energy $V_0(\rho_P)$ in CH_4 and C_2H_6 as a function of the reduced perturber number density ρ_r (i.e., $\rho_r = \rho_P/\rho_c$, where the critical density ρ_c is $6.1 \times 10^{21} \text{ cm}^{-3}$ for methane and $4.1 \times 10^{21} \text{ cm}^{-3}$ for ethane). The solid line and closed markers represent the calculation and experimental results for various noncritical temperatures, respectively; the dashed line and open markers are for an isotherm (-81.5°C for methane and 32.5°C for ethane) near the perturber critical isotherm. (\bullet , \circ and \blacktriangle) were measured in Cell 1, while (\blacksquare , \square) were measured in Cell 2.

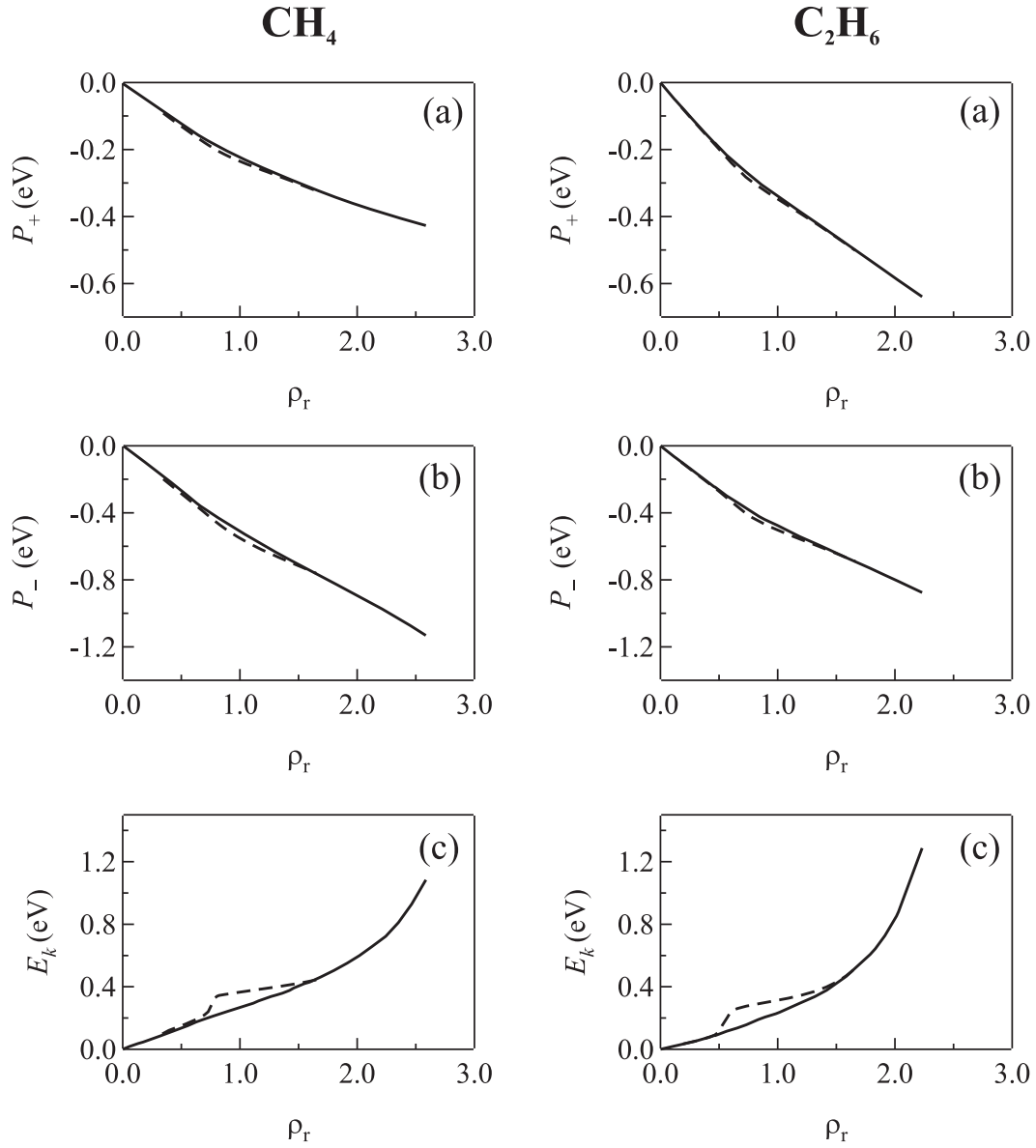


Fig. 4. The calculated (a) average ion/perturber polarization energies $P_+(\rho_P)$, (b) the average electron/perturber polarization energy $P_-(\rho_P)$, and (c) the zero-point kinetic energy $E_k(\rho_P)$ plotted as a function of the reduced density ρ_r in methane and ethane at noncritical temperatures (—) and on an isotherm near the critical isotherm (- - -) of the perturber. Parameters for the calculations are listed in Tables 1 and 2.

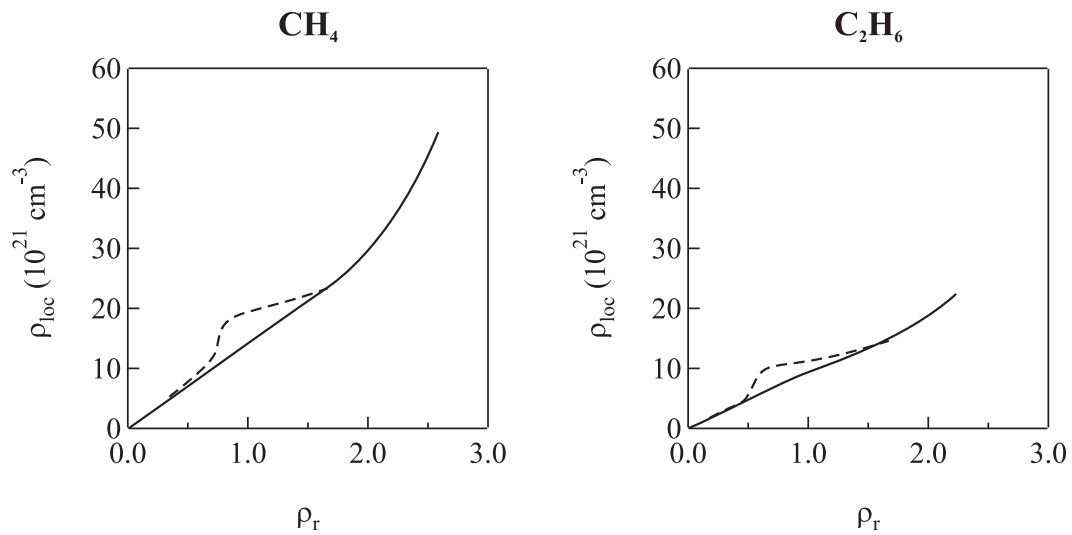


Fig. 5. The calculated local density ρ_{loc} plotted as a function of ρ_r in methane and ethane at noncritical temperatures (—) and on an isotherm near the critical isotherm (- - -) of the perturber.